

Freeze-in $SU(2)$ vector dark matter at low reheating temperature

Dilip Kumar Ghosh ^a, Sourav Gope ^b, Xiao-Gang He ^{c,d}, Xuan Hong ^{c,d}, Sk Jeesun ^{c,d}

^aSchool of Physical Sciences, Indian Association for the Cultivation of Science, 2A & 2B, Raja S.C. Mullick Road, Kolkata, West Bengal-700032, India

^bDepartment of Physics, Indian Institute of Technology Kharagpur, Kharagpur 721302, India

^cState Key Laboratory of Dark Matter Physics, Tsung-Dao Lee Institute & School of Physics and Astronomy, Shanghai Jiao Tong University, Shanghai 200240, China

^dKey Laboratory for Particle Astrophysics and Cosmology (MOE) & Shanghai Key Laboratory for Particle Physics and Cosmology, Shanghai Jiao Tong University, Shanghai 200240, China

E-mail: tpdkg@iacs.res.in, sourav@phy.iitkgp.ac.in, hexg@phys.ntu.edu.tw, hxxh123@sjtu.edu.cn, jeesun@sjtu.edu.cn

Abstract. The freeze-in mechanism for dark matter (DM) requires extremely feeble interactions with the Standard Model (SM), preventing thermal equilibrium in the early Universe and typically evading experimental detection. However, for sufficiently low reheating temperatures (T_{RH}), the observed relic abundance can be realized with larger couplings, opening prospects for experimental searches. In this work, we investigate freeze-in production of $SU(2)_{\text{HS}}$ vector dark matter (VDM) in a low- T_{RH} cosmology. The framework naturally contains three mass-degenerate stable VDM candidates without the need for any additional discrete symmetry. We perform a systematic study of the dark matter phenomenology and identify the parameter space consistent with the observed relic abundance. In contrast to conventional freeze-in scenarios, the required DM couplings can be sizable, rendering part of the parameter space already constrained by existing direct searches like PandaX-4T and LZ, while a significant region remains within the reach of future experiments such as DARWIN. Though one can realize the freeze-in mechanism for an abelian $U(1)_X$ vector DM models as well, we find that the non-abelian structure of the $SU(2)_{\text{HS}}$ scenario leads to a distinct feature due to a larger number of dark matter particles, resulting in an enlarged viable parameter space due to the multiplicity of dark matter states.

Contents

1	Introduction	1
2	Model	2
3	DM production	5
4	Results and constraints	8
5	Conclusion	12
A	Parametrization	13
B	Cross-sections for $h_i h_j \rightarrow XX$	14
C	Interaction Lagrangian of scalar sector	16

1 Introduction

Numerous observations at cosmological and astrophysical scales have established the presence of non-luminous non-baryonic dark matter (DM) component in the universe, saturating 25% of the total energy density of the universe [1–4]. Since the Standard Model (SM) lacks a viable DM candidate, various beyond-the-SM scenarios have been proposed [5–7]. A well-studied example is the weakly interacting massive particle (WIMP), where the relic abundance is set by thermal freeze-out with electroweak-scale interactions [8, 9]. However, null results from direct, indirect, and collider searches have significantly constrained the conventional WIMP paradigm [10–14]. Another widely explored alternative scenario is the *freeze-in* DM where extremely feeble couplings ($\lesssim \mathcal{O}(10^{-10})$) of DM prevent thermal equilibrium with the SM bath [15, 16]. In this scenario, DM is produced non-thermally via particle decays or annihilations, with an initial abundance that is negligible. Despite the elegance in the model construction, freeze-in DM models are notoriously difficult to test in the ongoing DM search experiments. Also, the ad hoc assumption of a negligible DM density in the early universe is now being seriously challenged [17].

It is interesting to note that the production of any species in the early universe is strongly dependent on the evolution of the universe. Recently, it has been shown that the assumption of a suppressed coupling of freeze-in DM can be significantly relaxed by invoking a low reheating temperature (T_{RH}) [17]. The reheating temperature is defined as the epoch when the inflaton field dilutes most of its energy density into the radiation bath, making it a subdominant component and creating a radiation-dominated universe. On the other hand, we have the precise information of a radiation-dominated universe only after the epoch of Big Bang Nucleosynthesis (BBN) at the temperature \sim few MeV [18, 19]. Hence, in principle, one can assume T_{RH} as low as $\mathcal{O}(10)$ MeV. In such a scenario, when the reheating temperature is smaller than the DM mass (m), only a sub-fraction of the particles annihilating to DM can potentially generate DM that lies in the tail of the Boltzmann distribution function with energy $\gg T_{\text{RH}}$ and the overall DM production rate becomes suppressed by $\exp(-m/T)$ [17]. Consequently, to satisfy the observed DM density, one needs to assume stronger DM

couplings compared to the vanilla freeze-in DM. This has a striking consequence in the detection aspects, making freeze-in DM discoverable in the next generation experiments while opening up a new viable parameter space for DM genesis, bridging the gap between the parameter spaces for freeze-out and vanilla freeze-in. In the past few years, several studies have explored this possibility for different models [20–28].

Motivated by this, in this work, we explore the freeze in production of $SU(2)$ vector DM (VDM) scenario at low reheating temperatures. We consider a minimal BSM model, where the SM particle content is augmented by a multiplet of spin-1 (vector) gauge bosons X_i ($i = 1, 2, 3$) associated with a hidden non-abelian gauge symmetry $SU(2)_{\text{HS}}$ [29, 30]. Note that all the SM particles are singlets under this new gauge group. The scalar sector of this BSM model includes a BSM scalar doublet ϕ whose vacuum expectation value (VEV) spontaneously breaks the $SU(2)_{\text{HS}}$, generating the mass of the DM candidate X . The striking feature of such a model is that the 3 DM candidates X_i become stable due to the custodial $SO(3)$ symmetry emerged from the $SU(2)_{\text{HS}}$ breaking without any imposition of additional discrete symmetry that is commonly found in other DM models. Due to the custodial symmetry, DM X_i always couples to the scalar ϕ in pairs, thereby forbidding the DM decay. In this setup, the DM interacts with the SM sector through the ϕ portal, which mixes with the SM Higgs, enabling an efficient DM production in the early universe from the SM bath. As mentioned earlier, we are interested in the paradigm where DM mass is larger than T_{RH} , which leads to a Boltzmann-suppressed freeze-in production rate. As a result, such a scenario requires a comparatively larger coupling, allowing us to explore a new parameter regime with rich phenomenological insights. Compared to $U(1)_X$ abelian vector DM, the VDM model considered in this work offers a distinct parameter space due to a larger number ($= 3$) of DM candidates. Also, from a model construction perspective $U(1)_X$ VDM model requires an ad hoc \mathcal{Z}_2 symmetry to forbid the kinetic mixing between $U(1)_X$ and the $U(1)_Y$ in the SM, so that the DM becomes stable [22]. We systematically analyze the production mechanism, considering all possible interactions, through numerical implementation. We also discuss possible theoretical and experimental constraints on such a model. The enhanced detection prospects of such non-thermal DM X in current direct detection experiments are also highlighted.

This paper is organized as follows. In Sec.2 we present the particle content and the basic setup. Sec.3 contains the details of obtaining the produced DM density and its dependencies on various model parameters. We discuss the theoretical and experimental constraints along with our numerical results in Sec.4. Finally, we conclude in Sec.5. Some relevant discussions about the scalar sector has been made in Appendix A, B, and C.

2 Model

We consider an extension of the Standard Model (SM) by a non-abelian gauge symmetry $SU(2)_{\text{HS}}$, under which the SM particles are singlets. The SM particle content is also augmented by a BSM scalar doublet ϕ , charged under this group. The DM candidates are the three gauge bosons of this group, represented by X_i ($i = 1, 2, 3$). The DM can interact with the SM particles through a Higgs-portal interaction. The Lagrangian of this model is written as, [29]:

$$\mathcal{L}_{\text{BSM}} \supset -\frac{1}{4}V^{a\mu\nu}V_{\mu\nu}^a + (D_\mu\phi)^\dagger(D^\mu\phi) - V(H, \phi) \quad (2.1)$$

where $D^\mu\phi = (\partial^\mu - ig_\phi\frac{\tau^a}{2}X^{a\mu})\phi$ with g_ϕ is the $SU(2)_{\text{HS}}$ gauge coupling; and τ^a are the Pauli matrices. The field tensor of the BSM gauge boson is depicted by, $V_{\mu\nu}^a = \partial_\mu X_\nu^a - \partial_\nu X_\mu^a + g_\phi\epsilon^{abc}X_\mu^bX_\nu^c$, where the $SU(2)$ indices a, b, c run from 1 – 3. H represents the SM Higgs doublet charged under the SM gauge group. The scalar sector of the framework reads as,

$$V(H, \phi) = \mu_H^2(H^\dagger H) + \lambda_H(H^\dagger H)^2 + \mu_\phi^2\phi^\dagger\phi + \lambda_\phi(\phi^\dagger\phi)^2 + \lambda_{\phi H}\phi^\dagger\phi H^\dagger H \quad (2.2)$$

For the spontaneous symmetry breaking in both sectors (SM & $SU(2)_{\text{HS}}$) one requires $\mu_H^2 < 0$ and $\mu_\phi^2 < 0$. In the unitary gauge one can write H and ϕ as

$$H = \begin{pmatrix} 0 \\ \frac{v+S}{\sqrt{2}} \end{pmatrix}, \quad \phi = \begin{pmatrix} 0 \\ \frac{v_\phi+\phi_0}{\sqrt{2}} \end{pmatrix}. \quad (2.3)$$

where S and ϕ_0 are physical scalars after the SSB in both the SM and hidden sectors, respectively. v and v_ϕ denote the vacuum expectation values along the SM Higgs and hidden-scalar directions, respectively. Thus, the hidden sector gauge boson X becomes massive by absorbing the Goldstone degrees of freedom of the $SU(2)_{\text{HS}}$ Higgs field ϕ and the corresponding Lagrangian is given by,

$$\begin{aligned} \mathcal{L}_{\text{int}} \supset & -\frac{1}{4}V^{a\mu\nu}V_{\mu\nu}^a + \frac{1}{2}(\frac{1}{2}g_\phi v_\phi)^2 X_\mu^a X^{a\mu} + \frac{1}{4}g_\phi^2 v_\phi X_\mu^a X^{a\mu} \phi_0 + \frac{1}{8}g_\phi^2 X_\mu X^\mu \phi_0^2 \\ & -\frac{1}{2}\lambda_{\phi H}(v_\phi + \phi_0)^2 H^\dagger H + \mathcal{L}_{\phi_0}, \end{aligned} \quad (2.4)$$

where,

$$\mathcal{L}_{\phi_0} = \frac{1}{2}(\partial_\mu\phi_0)(\partial^\mu\phi_0) - \frac{1}{2}\mu_\phi^2(v_\phi + \phi_0)^2 - \frac{1}{4}\lambda_\phi(v_\phi + \phi_0)^4. \quad (2.5)$$

The spontaneous breaking of $SU(2)_{\text{HS}}$ has several important consequences. First, all three hidden gauge bosons acquire a common mass, $m_X = \frac{1}{2}g_\phi v_\phi$. Second, the symmetry-breaking pattern leaves an accidental custodial $SO(3)$ symmetry acting on the triplet of hidden gauge bosons X_μ^a , with $a = 1, 2, 3$. As a result, the three vector states remain exactly mass-degenerate. Moreover, the custodial $SO(3)$ invariance implies that the hidden gauge bosons enter the scalar interaction terms only through $SO(3)$ -singlet combinations such as $X_\mu^a X^{a\mu}$. Consequently, no interaction vertex involving a single X_μ^a is generated after symmetry breaking, and the lightest hidden vector states are stable. Thus, the three components $X_\mu^{1,2,3}$ collectively constitute a triply degenerate vector dark matter sector, with identical masses and portal interactions. This stability arises dynamically from the residual custodial symmetry and does not require the imposition of an additional ad hoc \mathcal{Z}_2 symmetry, unlike many Abelian vector dark matter constructions. For example, $U(1)_X$ abelian VDM model would require the BSM gauge boson and a BSM singlet scalar to transform non-trivially under this \mathcal{Z}_2 , while all the SM fields transform trivially under the same \mathcal{Z}_2 [22]. Such a symmetry forbids the kinetic mixing of the $U(1)_X$ vector boson and the $U(1)_Y$ gauge boson, which is crucial to make the DM stable.

After electroweak symmetry breaking (EWSB), the CP-even scalar component of the SM Higgs doublet, S , mixes with the CP-even hidden-sector scalar (ϕ_0). The minimization condition of the entire potential i.e. $\partial V(H, \phi)/\partial\phi_0 = 0 = \partial V(H, \phi)/\partial S$ leads to,

$$\mu_H^2 = -\lambda_H v^2 - \frac{1}{2}\lambda_{\phi H} v_\phi^2, \quad \mu_\phi^2 = -\lambda_\phi v_\phi^2 - \frac{1}{2}\lambda_{\phi H} v^2 \quad (2.6)$$

Thus, the mass matrix of the CP even scalars $(S \ \phi_0)^T$ is given by,

$$M^2 = \begin{pmatrix} 2\lambda_H v^2 & \lambda_{\phi H} v v_\phi \\ \lambda_{\phi H} v v_\phi & 2\lambda_\phi v_\phi^2 \end{pmatrix} \quad (2.7)$$

Upon diagonalization the physical scalar (h, η) masses are given by,

$$m_{h,\eta}^2 = \lambda_H v^2 + \lambda_\phi v_\phi^2 \mp \sqrt{(\lambda_H v^2 - \lambda_\phi v_\phi^2)^2 + \lambda_{\phi H}^2 v^2 v_\phi^2}, \quad (2.8)$$

In our convention, h represents the SM Higgs boson with mass $m_h = 125$ GeV. In equation 2.8, $-(+)$ sign corresponds to $m_h(m_\eta)$ for the case $m_h < m_\eta$. Conversely, for $m_h > m_\eta$, corresponding masses are obtained by interchanging the \pm signs in the same equation. h, η is related to the unphysical basis by,

$$\begin{pmatrix} h \\ \eta \end{pmatrix} = \begin{pmatrix} \cos \beta & -\sin \beta \\ \sin \beta & \cos \beta \end{pmatrix} \begin{pmatrix} S \\ \phi_0 \end{pmatrix}, \quad \text{with, } \tan 2\beta = \frac{\lambda_{\phi H} v v_\phi}{\lambda_\phi v_\phi^2 - \lambda_H v^2} \quad (2.9)$$

Thus, the main interaction channel of X is through the Higgs portal (h, η) with SM fermions and the SM gauge bosons governed by $\sin 2\beta \times (g_\phi v_\phi)$, which is important from both production and detection aspects. Also there can be quartic vertex with h, η governed by $\sin \beta(\cos \beta) \times g_\phi$ and scalar portal interactions of $hh(\eta\eta) \rightarrow XX$ governed by same $\sin \beta$ and $(g_\phi v_\phi)$. The relevant Feynman diagrams related for DM production are shown in Fig.1. The model parameters are the following:

$$m_X, g_\phi, \sin \beta, m_\eta \quad (2.10)$$

Since X is the DM candidate, we use M_{DM} and m_X interchangeably. The other dependent variables in terms of these independent parameters can be found in Appendix A.

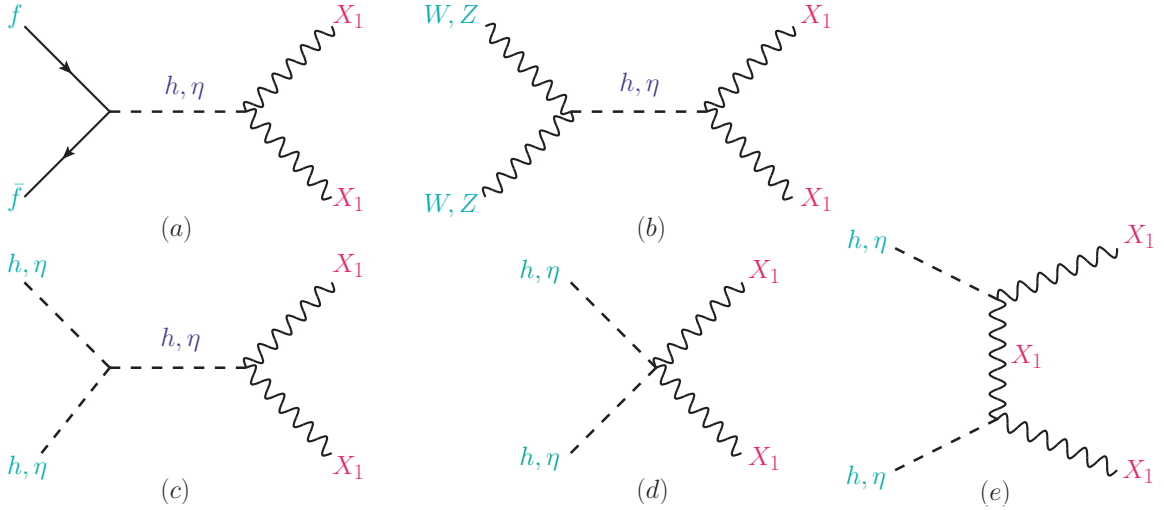


Figure 1. Feynman diagrams relevant for DM production. The channels are (a) fermion annihilation via scalar mediator, (b) gauge boson annihilation via scalar mediator, (c) scalar annihilation via scalar mediator, (d) scalar annihilation w/o mediator, (e) scalar annihilation via VDM mediator. For the last one, there also exists a u -channel diagram, which is not shown explicitly.

3 DM production

Following the detailed discussion of the BSM model in the previous section, we are now set to analyze the freeze in DM production in the early universe. As mentioned in the Introduction, the reheating temperature T_{RH} is one of the key inputs that governs the freeze-in abundance, which will be shown in this section. The DM X gets produced from the BSM interactions of SM particles as well as the BSM scalar η . The evolution of X density can be obtained by solving the Boltzmann equation as a function of temperature T ,

$$\begin{aligned} \frac{dY_X}{dT} = & -\frac{S_{\text{ent}}}{HT} \sum_{i=f,h,\eta,V} [(Y_i^{eq})^2 \langle \sigma v \rangle_{ii \rightarrow XX} - (Y_X)^2 \langle \sigma v \rangle_{XX \rightarrow ii}] \\ & -\frac{1}{HT} \sum_{j=h,\eta} [(Y_j^{eq} \langle \Gamma \rangle_{j \rightarrow XX} - Y_X \langle \Gamma \rangle_{XX \rightarrow j})], \end{aligned} \quad (3.1)$$

where, Y_X and Y_i^{eq} signify the comoving number density of DM X and comoving equilibrium number density of the species i ($\equiv f, h, V, \eta$). Moreover, S_{ent} stands for the comoving entropy density, whereas $H = \sqrt{8\pi\rho_{\text{rad}}/3}/M_{\text{pl}}$ is the Hubble expansion rate with M_{pl} and ρ_{rad} being the Planck mass and the total energy density, respectively. The initial condition is imposed by setting $Y_X = 0$ at $T = T_{\text{RH}}$. Note that the total DM abundance Y_{DM} can be obtained by adding the abundances of different DM species i.e. $Y_{\text{DM}} = 3Y_X$. Here, the multiplication factor 3 implies the three components of X_i ($i = 1, 2, 3$).

The right-hand side (RHS) of the aforementioned equation encodes the collision terms with all the relevant interactions as shown in Fig.1. The term in the first line in the RHS corresponds to the annihilation of SM particles (fermions, gauge bosons, and Higgs) as well as the BSM scalar η . The second term in the same first line takes care of the possible back-reaction of X and the subsequent dilution of X . However, the second contribution is practically negligible given the very small initial abundance of X . On the other hand, the term in the second line in the RHS contains the contribution from the decay of the scalar particle j ($\equiv h, \eta$) when $2m_X \leq m_j$. The thermal averages of the respective annihilation cross section (σ) and decay width (Γ) are denoted by $\langle \sigma v \rangle$ and $\langle \Gamma \rangle$, respectively. The production cross sections for pair annihilation of SM fermions and gauge bosons are given as,

$$\begin{aligned} \sigma_{f\bar{f} \rightarrow XX} = & \frac{1}{N_c} \frac{m_f^2 \sin^2 2\beta}{256\pi s v^2 v_\phi^2} \left| \frac{1}{s - m_h^2 + im_h \Gamma_h} - \frac{1}{s - m_\eta^2 + im_\eta \Gamma_\eta} \right|^2 (s^2 - 4m_X^2 s + 12m_X^4) \\ & \sqrt{(s - 4m_f^2)(s - 4m_X^2)} \end{aligned} \quad (3.2)$$

$$\begin{aligned} \sigma_{VV \rightarrow XX} = & \frac{\sin^2 2\beta}{1152\pi s v^2 v_\phi^2} \left| \frac{1}{s - m_h^2 + im_h \Gamma_h} - \frac{1}{s - m_\eta^2 + im_\eta \Gamma_\eta} \right|^2 (s^2 - 4m_X^2 s + 12m_X^4) \\ & \times (s^2 - 4m_V^2 s + 12m_V^4) \sqrt{\frac{(s - 4m_X^2)}{(s - 4m_V^2)}}. \end{aligned} \quad (3.3)$$

m_f (m_V) signifies the mass of SM fermion (gauge boson i.e. Z, W^\pm) and N_c stands for the color factor. Note that $N_c = 3$ for quarks and $N_c = 1$ for leptons. Apart from these, there also exist scattering processes like hh ($\eta\eta$) $\rightarrow XX$ and $h\eta \rightarrow XX$ which are summarized in Appendix A. Finally, the decay widths are given by,

$$\Gamma(h \rightarrow X_i X_i) = \frac{g_\phi^2 m_h^3 \sin^2 \beta}{128\pi m_X^2} \sqrt{1 - 4\frac{m_X^2}{m_h^2}} \left\{ 1 - 4\frac{m_X^2}{m_h^2} + 12\frac{m_X^4}{m_h^4} \right\} \quad (3.4)$$

$$\Gamma(\eta \rightarrow X_i X_i) = \frac{g_\phi^2 m_\eta^3 \cos^2 \beta}{128\pi m_X^2} \sqrt{1 - 4 \frac{m_X^2}{m_\eta^2}} \left\{ 1 - 4 \frac{m_X^2}{m_\eta^2} + 12 \frac{m_X^4}{m_\eta^4} \right\} \quad (3.5)$$

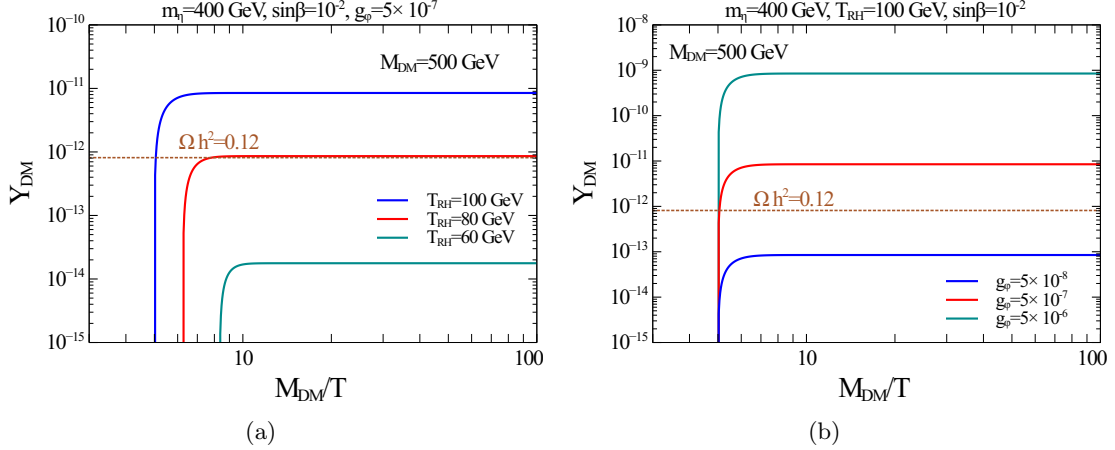


Figure 2. Evolution of co-moving number densities of DM Y_{DM} with respect to M_{DM}/T for a benchmark $m_\eta = 400$ GeV, and $\sin\beta = 10^{-2}$. **Left:** Variation of Y_{DM} with different values of T_{RH} for a fixed coupling $g_\phi = 5 \times 10^{-7}$. The cyan, red and blue lines correspond to $T_{\text{RH}} = 60$ GeV, 80 GeV and 100 GeV, respectively. **Right:** Variation of Y_{DM} with different values of g_ϕ for a fixed $T_{\text{RH}} = 100$ GeV. The cyan, red and blue lines correspond to $g_\phi = 5 \times 10^{-8}$, 5×10^{-7} and 5×10^{-6} , respectively.

We numerically solve eq.(3.1) and show the evolution of comoving abundance of DM with respect to M_{DM}/T in Fig.2. For this plot, we consider a benchmark value of model parameters $m_\eta = 400$ GeV, $\sin\beta = 10^{-2}$. In Fig.2(a) we display the comoving abundances for different values of $T_{\text{RH}} = 60$ GeV, 80 GeV and 100 GeV for a fixed value of $g_\phi = 5 \times 10^{-7}$ depicted by cyan, red, and blue solid lines, respectively. As expected, starting from a negligible abundance, X promptly gains its freeze-in density around T_{RH} . Note that, with a decrease in T_{RH} , the abundance also decreases. This can be understood from the temperature dependence of the interaction rates encoded in $\langle\sigma v\rangle$ and $\langle\Gamma\rangle$. For example $\langle\sigma v\rangle$ reads as

$$\langle\sigma v\rangle = \frac{g_i^2 T}{2(2\pi)^4 (n_i^{eq})^2} \int_{\text{Max}[4m_X^2, 4m_i^2]}^{\infty} ds \sigma(s - 4m_f^2) \sqrt{s} K_1\left(\frac{\sqrt{s}}{T}\right), \quad (3.6)$$

where i signifies the particle participating in the DM production. g_i and n_i represent the degree of freedom and density of the particle i . Note that, in the limit $T \ll m_X$ the integration in the above equation is maximized when $s = 4m_X^2$ for $m_X > m_i$. In this limit, the Bessel function also behaves as $K_1(\sqrt{s}/T) \propto \sqrt{T/s^{1/2}} e^{-\sqrt{s}/T}$. Thus, with an increase in the ratio m_X/T_{RH} , the interaction rate and consequently Y_{DM} become exponentially suppressed as observed in Fig.2(a). This maps the physical scenario where the interaction rate samples only the high-energy tail of the thermal distribution of bath particles as T_{RH} decreases, leading to a decrease in the yield. In Fig.2(b) we showcase the variation Y_{DM} with different values of g_ϕ for a fixed $T_{\text{RH}} = 100$ GeV, the cyan, red, and blue lines correspond to $g_\phi = 5 \times 10^{-8}$, 5×10^{-7} and 5×10^{-6} . Needless to say, with an increase in the coupling g_ϕ , the relevant collision terms increase as $\sim g_\phi^2$, leading to an enhanced density of DM. In other

words, it can be stated that to satisfy the same DM abundance, the associated DM couplings should be higher for a lower value of T_{RH} . This crucial feature serves as the primary focus of this work. It is also worth highlighting that even with the same value of associated DM cross-section, the obtained DM abundance Y_{DM} in this model is higher (by a factor 3) than other Higgs portal $U(1)_X$ VDM models [22]. This feature helps to explore a new parameter space with new phenomenological aspects, as will be shown later on.

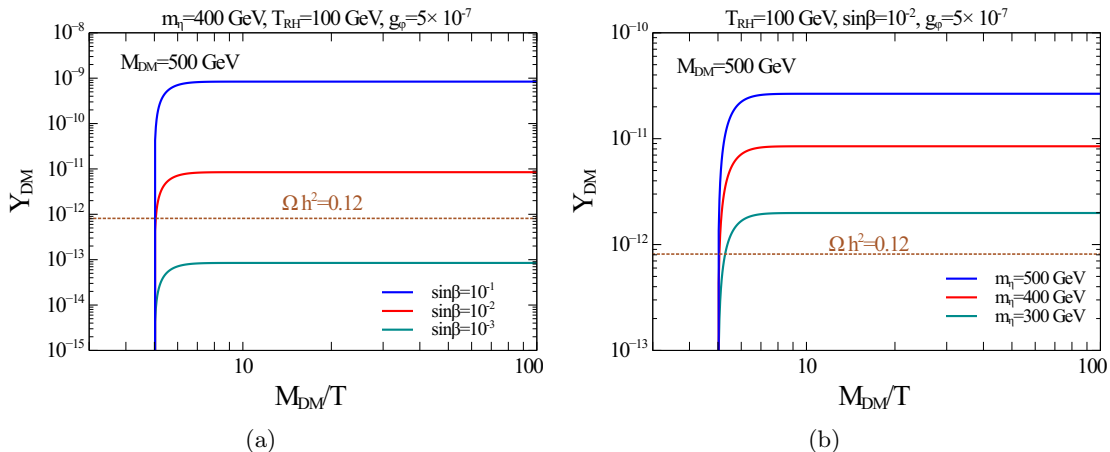


Figure 3. Evolution of co-moving number densities of DM Y_{DM} with respect to M_{DM}/T for a benchmark $T_{\text{RH}} = 100$ GeV and $g_\phi = 5 \times 10^{-7}$. **Left:** Variation of Y_{DM} with different values of $\sin \beta = 10^{-1}, 10^{-2}, 10^{-3}$ depicted by cyan, red, and blue lines, respectively, for a fixed $m_\eta = 400$ GeV. **Right:** Variation of Y_{DM} with different values of m_η for a fixed $\sin \beta = 10^{-2}$. The cyan, red and blue lines correspond to $m_\eta = 300$ GeV, 400 GeV and 500 GeV, respectively.

We analyze the dependence of DM density on other model parameters in Fig.3. For this plot, we now take the fixed values of $T_{\text{RH}} = 100$ GeV and $g_\phi = 5 \times 10^{-7}$. In Fig.3(a) we display the comoving abundances for different values of $\sin \beta = 10^{-1}, 10^{-2}, 10^{-3}$ for a fixed value of $m_\eta = 400$ GeV depicted by cyan, red, and blue solid lines, respectively. One can observe that the DM abundance increases with $\sin \beta$ as the cross-section has explicit dependence on it, which essentially enhances the collision terms that generate the DM density. On the other hand, in Fig.3(b) we showcase the comoving abundances for different values of $m_\eta = 300$ GeV, 400 GeV and 500 GeV for a fixed value of $\sin \beta = 10^{-2}$ depicted by cyan, red, and blue solid lines, respectively. Here, one can surmise that higher values of m_η correspond to a higher abundance of DM. This trend should be understood as a result of the combined m_η -dependence of the scalar cross-section/decay, mediator propagators, interference effects, and thermal phase-space integrals. Indeed the scalar-annihilation channels, such as $\eta\eta \rightarrow X_i X_i$ and $h\eta \rightarrow X_i X_i$, increasing m_η can increase the typical \sqrt{s} and hence leads to a Boltzmann suppression through $K_1(\sqrt{s}/T)$. However, the growth of Y_{DM} with m_η is not a purely kinematic phase-space effect, but rather a benchmark-dependent result due to the interplay among scalar amplitudes and thermal suppression factors.

After having a detailed discussion on the dependencies of DM density on various model parameters, we will discuss the phenomenological aspects of such a setup through comprehensive numerical analysis.

4 Results and constraints

In the previous section, we argued that a low $T_{\text{RH}} (< m_{\text{DM}})$ requires a higher value of DM coupling to satisfy the observed relic density. In this section, we perform exhaustive numerical scans over various model parameters to understand phenomenological implications. However, the BSM extension of a singlet scalar ϕ and three X_i particles can have important implications on various existing experimental data. Hence, to ensure phenomenological viability, it is essential to critically examine the aforementioned BSM scenario in light of existing experimental data. In addition to that, theoretical consistency imposes additional constraints, requiring the model parameters to satisfy a set of well-defined conditions. Before delving into the numerical analysis, we briefly discuss the existing constraints on the model parameters.

Theoretical constraints: The model parameters are constrained by perturbative unitarity, perturbativity, and vacuum stability. The unitarity of scalar scattering amplitudes imposes the following conditions:

$$|\lambda_{\phi H}| \leq 8\pi, \quad |\lambda_H| \leq 4\pi, \quad |\lambda_\phi| \leq 4\pi, \quad (4.1)$$

$$|3(\lambda_H + \lambda_\phi) \pm \sqrt{9(\lambda_H - \lambda_\phi)^2 + 4\lambda_{\phi H}^2}| \leq 8\pi. \quad (4.2)$$

Furthermore, perturbativity and the requirement of the scalar potential to be bounded from below further imply,

$$\lambda_H > 0, \quad \lambda_\phi > 0, \quad \lambda_{\phi H} > -2\sqrt{\lambda_H \lambda_\phi}. \quad (4.3)$$

The quartic couplings as a function of the scalar masses can be found in Appendix A.

Collider bounds: In the present setup, the SM Higgs boson couples to both the DM X and the other physical neutral scalar η (eq. (2.4)). Thus, in the kinematically allowed mass hierarchy, the SM Higgs can decay to these BSM channels, contributing to the invisible decay. Hence, one very important bound can come from the measurements of the invisible decay width of the SM Higgs. For $m_h > 2m_X$, the Higgs can decay invisibly into DM particles, with total width

$$\Gamma_{\text{inv}} = \sum_{i=1}^3 \Gamma(h \rightarrow X_i X_i) = 3 \Theta(m_h - 2m_X) \frac{g_\phi^2 m_h^3 \sin^2 \beta}{128\pi m_X^2} \sqrt{1 - \frac{4m_X^2}{m_h^2}} \left(1 - \frac{4m_X^2}{m_h^2} + 12 \frac{m_X^4}{m_h^4}\right). \quad (4.4)$$

In addition, the Higgs can decay into η pairs with a decay width

$$\Gamma(h \rightarrow \eta\eta) = \Theta(m_h - 2m_\eta) \frac{\rho_1^2}{32\pi m_h} \sqrt{1 - \frac{4m_\eta^2}{m_h^2}}. \quad (4.5)$$

If kinematically allowed, both channels contribute to the BSM width, denoted by Γ_{BSM} . The total Higgs decay width is then given by

$$\Gamma_h = \Gamma_{\text{BSM}} + \cos^2 \beta \Gamma_h^{\text{SM}}, \quad (4.6)$$

where $\Gamma_h^{\text{SM}} = 4.2$ MeV is the total decay width of the Higgs boson into SM particles [31]. The branching fraction into BSM states is constrained to satisfy

$$\mathcal{B}_{\text{BSM}} \leq 0.47, \quad (4.7)$$

and the total Higgs width is required to lie within the range

$$1.0 \text{ MeV} < \Gamma_h < 6.0 \text{ MeV}. \quad (4.8)$$

These conditions impose constraints on g_ϕ and $\sin\beta$ for a benchmark m_X and m_η . Apart from the invisible decay, Higgs signal strength measurements impose a weaker constraint on mixing angle, which restricts $\sin\beta < 0.23$ [32].

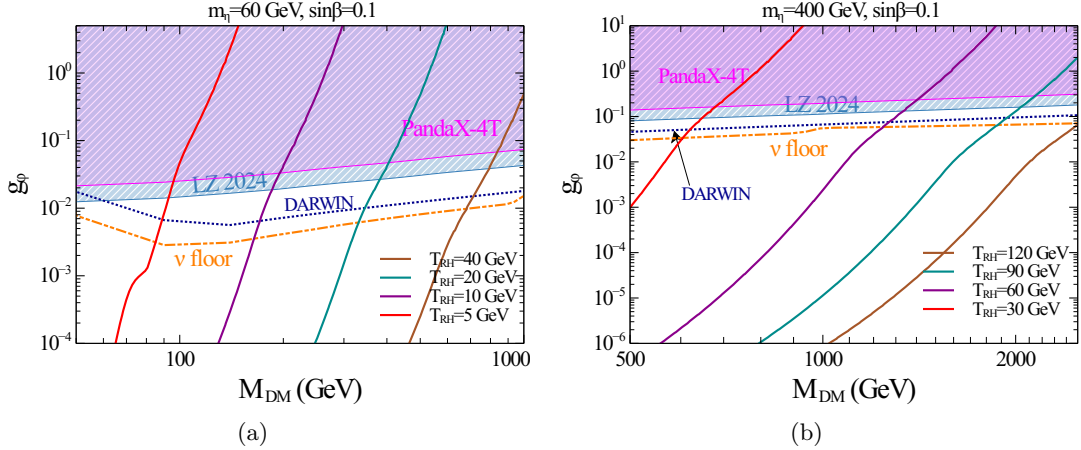


Figure 4. Contours satisfying the observed relic density are shown in the $g_\phi - M_{\text{DM}}$ plane. Different contours correspond to varying reheating temperatures T_{RH} . The direct detection limits from the LZ 2024 experiment are overlaid as exclusion bounds. The panel (a) and (b) correspond to $m_\eta = 60 \text{ GeV}$ and 400 GeV respectively. In both cases, the scalar mixing angle is fixed to $\sin\beta = 0.1$.

Direct detection: A direct detection experiment can potentially provide the direct signal of an incoming DM. While the Earth passes through the galactic DM halo, DM particles are expected to scatter target nucleons in Xenon-based detectors, providing a distinct recoil signal. Null observation of any such recoil signal stringently constrains the DM nucleon elastic scattering cross-section. The DM candidate X interacts with nucleons via scalar mediation through the Higgs boson h and the scalar η . The resulting spin-independent (SI) scattering cross section is given by

$$\sigma_{\text{SI}} = \frac{1}{64\pi} f^2 m_N^2 \frac{v_\phi^2}{v^2} g_\phi^4 \sin^2(2\beta) \frac{(m_\eta^2 - m_h^2)^2}{m_\eta^4 m_h^4} \frac{\mu_r^2}{m_X^2}, \quad (4.9)$$

where $\mu_r = \frac{m_N m_X}{m_N + m_X}$ denotes the reduced mass of the DM–nucleon system, and f parametrizes the effective Higgs–nucleon coupling given as,

$$f \equiv \frac{\langle N | \sum_q \bar{q}q | N \rangle}{m_N} \quad (4.10)$$

We take the value $f = 0.3$. For this work, we consider the existing constraints from experiments like LZ [33], PandaX-4T [34] (Fig. 4).

Indirect detection: DM can pair annihilate into SM particles via h and η portal interactions. The null observation of any excess signal in different space-based or ground-based telescopes strongly constrains such annihilation channels. For our analysis, the relevant indirect detection constraint comes from the DM annihilation to gauge bosons and quarks. We discuss such bounds on $X_i X_i \rightarrow W^+ W^-$ channel from the FERMI-LAT [35] and AMS [36] experiments, which are found to be strongest (Fig. 6).

Results: We present contour plots satisfying the observed DM relic abundance in the $M_{\text{DM}}-g_\phi$ plane in figure 4. The DM relic abundance is estimated from Y_{DM} ,

$$\Omega h^2 = 2.755 \times 10^8 Y_{\text{DM}} (m_{\text{DM}}/\text{GeV}). \quad (4.11)$$

We vary the DM mass and coupling for two benchmark mediator masses, $m_\eta = 60$ GeV (**left**) and 400 GeV (**right**), and fixed mixing angle $\sin \beta = 0.1$. Note that the chosen benchmark is allowed by the theoretical constraints and collider bounds [30]. The different colored solid lines correspond to different values of T_{RH} that satisfy the observed relic density $\Omega h^2 = 0.12$ [4]. In the left plot, the red, dark magenta, cyan, and brown solid lines signify $T_{\text{RH}} = 5$ GeV, 10 GeV, 20 GeV, and 40 GeV, respectively. On the other hand, in the right plot, the red, dark magenta, cyan, and brown solid lines signify $T_{\text{RH}} = 30$ GeV, 60 GeV, 90 GeV, and 120 GeV, respectively. In both panels, it is observed that for a fixed DM mass, a larger gauge coupling g_ϕ is required to reproduce the correct relic density as the reheating temperature T_{RH} decreases. This behaviour follows from the exponential suppression of the DM production rate at lower T_{RH} , as indicated in eq. (3.6). Consequently, a larger coupling is required to compensate for the suppressed production and yield the observed relic abundance. In the same plane, we display 90% confidence limit (C.L.) direct detection constraints from LZ [33], PandaX-4T [34] depicted by the light blue hatched region and magenta shaded region, respectively. Due to the enhanced couplings in low T_{RH} , we find a large portion of the parameter space is excluded. We also showcase the potential future sensitivity from DARWIN [37] and the neutrino floor represented by the blue dotted line and the orange dashed dot line, respectively. Despite the stringent constraints, there still remains an allowed parameter space for such freeze-in DM that can be tested in future experiments like DARWIN. Also, major parts of the relic satisfy the contours lie below the neutrino floor.

In Fig.5 we highlight the importance of the 3 components of VDM particles realized in this $SU(2)_{\text{HS}}$ model. In this plot We show the variation in DM-nucleon cross-section (σ_{SI}) with the DM mass for a fixed benchmark mediator masses, $m_\eta = 60$ GeV and mixing angle $\sin \beta = 0.1$, considering two different values of reheating temperature $T_{\text{RH}} = 5$ GeV (left) and $T_{\text{RH}} = 10$ GeV (right) represented by red and magenta lines respectively. In the same plane, we display the relic satisfying contour for the same set of benchmark parameters with only one component of DM (say X_1) represented by the dotted lines. Note that, for a single component of DM (dotted line), a higher value of cross-section is required to satisfy the relic density for the same DM mass. However, the direct detection rate depends only on the total DM density at the present day, independent of the number of components. Hence, the direct detection constraints remain similar for both cases. In such a scenario, the $SU(2)_{\text{HS}}$ model can exhibit a larger allowed parameter space than that with a single DM component (e.g. $U(1)_X$ abelian VDM [22]). For example, with $T_{\text{RH}} = 5$ GeV (10 GeV) DM mass up to 92 GeV (184 GeV) is allowed from LZ 2024 in $SU(2)_{\text{HS}}$ scenario, whereas for the other scenario, DM mass only up to 89 GeV (180 GeV) is allowed. A similar conclusion can be drawn for the detection prospects in future experiments like DARWIN.

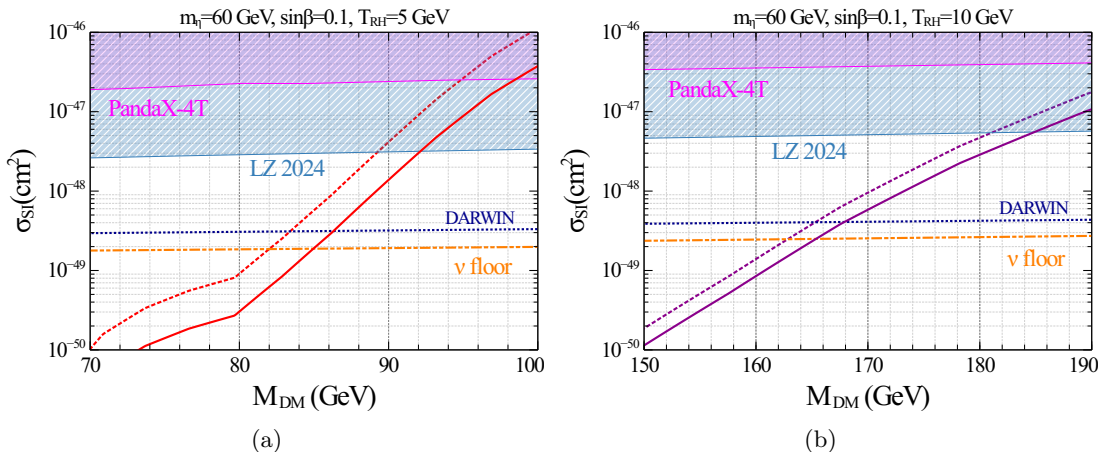


Figure 5. Direct search: comparison between the two DM cases for (a) $T_{\text{RH}} = 5$ GeV and (b) $T_{\text{RH}} = 10$ GeV. Solid lines represent the parameter space for VDM in $SU(2)_{\text{HS}}$ model and dotted lines represent the $U(1)_X$ model, respectively.

For the same set of benchmark parameters, we display the indirect detection constraints in Fig.6. Here also we fix $m_\eta = 60$ GeV (**left**) and 400 GeV (**right**), and fixed mixing angle $\sin\beta = 0.1$. Similar to the previous discussion, in the left plot, the red, dark magenta, cyan, and brown solid lines signify $T_{\text{RH}} = 5$ GeV, 10 GeV, 20 GeV, and 40 GeV, respectively. On the other hand, in the right plot, the red, dark magenta, cyan, and brown solid lines signify $T_{\text{RH}} = 30$ GeV, 60 GeV, 90 GeV, and 120 GeV, respectively. For a fixed value of g_ϕ , increasing the DM mass leads to a smaller annihilation cross section and hence a reduced relic abundance. As a result, a higher reheating temperature is required to reproduce the observed relic density. We have shown the 90% C.L. bounds on the thermal average cross-section for the process $X_i X_i \rightarrow W^+ W^-$ from the Fermi-LAT [35] and AMS [36] experiments depicted by magenta and light blue shaded regions. The Fermi-LAT [35] and AMS-02 [36] constraints are obtained by looking at the positron flux and the antiproton excess, respectively. The top-most points for each colored line satisfying the observed limit correspond to the perturbative limit on g_ϕ , and we do not extend the lines above that. For the chosen set of BP, the relic-satisfying contours lie below the existing indirect-detection constraints. Indirect-detection constraints from other channels, such as $b\bar{b}$ and $\mu\bar{\mu}$, are found to set weaker limits on $\langle\sigma v\rangle$, and hence we do not show them for brevity.

Another notable feature arises in this regime where the reheating temperature is smaller than the DM mass, which has a significant impact on the required gauge coupling. In the left panel of figure 4, the maximum allowed value of g_ϕ is $\mathcal{O}(10^{-2})$ for $M_{\text{DM}} \sim 100$ GeV, increasing to $\mathcal{O}(10^{-1})$ for $M_{\text{DM}} \sim 1$ TeV. In the right panel, g_ϕ can reach values as large as $\mathcal{O}(1)$ for $M_{\text{DM}} \sim 3$ TeV within the region allowed by direct detection constraints. Such coupling strengths are considerably larger than those typically encountered in conventional freeze-in scenarios. Consequently, these relatively large couplings are subject to stringent constraints from direct detection experiments, while simultaneously providing promising prospects for future detection.

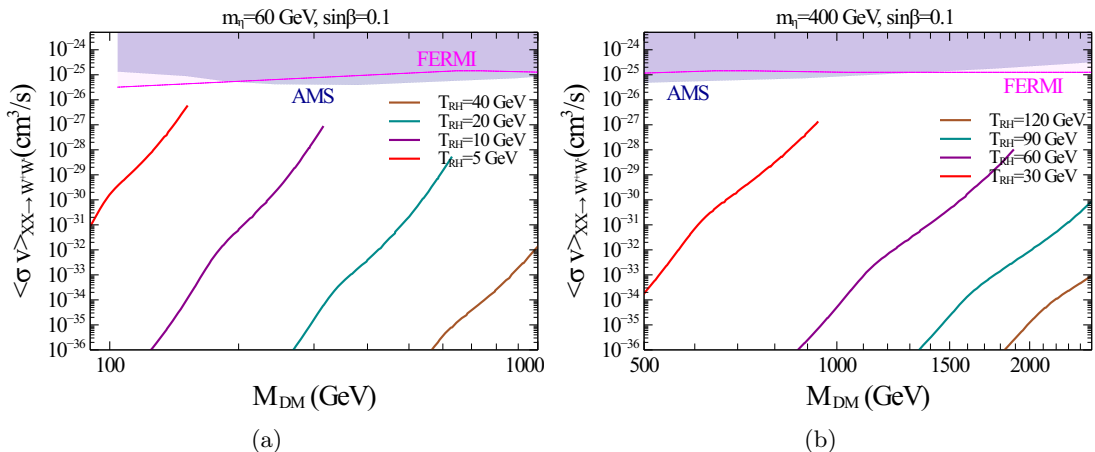


Figure 6. Contours satisfying the observed relic density are shown in the thermal average annihilation cross-section ($\langle\sigma v\rangle$) of DM to W^+W^- vs. M_{DM} plane with the different lines corresponding to the different T_{RH} similar to figure 4. Indirect detection bounds from the *Fermi*-LAT and AMS experiments are shown. The left and right panels correspond to the same parameter choices as in figure 4.

5 Conclusion

In this work, we consider a minimal beyond-the-Standard-Model (BSM) scenario where the SM particle spectrum is augmented by a hidden non-Abelian gauge symmetry $SU(2)_{\text{HS}}$, giving rise to three spin-1 gauge bosons $X_i (i = 1, 2, 3)$. The scalar sector includes an $SU(2)_{\text{HS}}$ doublet scalar ϕ which is neutral under the SM gauge group but carries a charge under the hidden gauge symmetry. The spontaneous breaking of $SU(2)_{\text{HS}}$ via the vacuum expectation value of ϕ generates a common mass for the three vector bosons, while the resulting $SO(3)$ custodial symmetry ensures their stability, allowing them to serve as vector dark matter candidates with the Higgs portal interactions with SM particles.

Within this framework, we study the freeze in production of VDM X_i at reheating temperatures lower than DM mass ($T_{\text{RH}} < M_{\text{DM}}$). In this limit, the DM phenomenology has a strong dependence on T_{RH} in contrast to the usual freeze-in scenario since the production (SM SM $\rightarrow X_i X_i$) rate of X_i suffers from a Boltzmann suppression ($\sim \exp(-m_{\text{DM}}/T_{\text{RH}})$). Consequently, one needs to consider higher values of DM couplings than usual freeze-in DM to overcome the Boltzmann suppression and obtain the correct relic density. This, in turn, helps to realize a freeze in DM with comparatively stronger coupling that can be testable in current and future generation DM search experiments, which serves as the key focus of this work.

We explicitly check the dependencies of DM abundance on various model parameters by solving the Boltzmann equation numerically, considering all relevant production channels. We find that with higher gauge coupling (g_ϕ) and the mixing angle ($\sin\beta$), the DM abundances increase as these parameters directly control the production cross-section. More importantly, we notice that with an increase by a few factors in the ratio $m_{\text{DM}}/T_{\text{RH}}$, the DM abundances decrease by a few orders of magnitude due to the previously mentioned Boltzmann suppression. To compensate for this suppression, the correct relic density is obtained with a comparatively larger coupling than that used in the usual freeze-in scenario. For example, for $m_{\text{DM}} \sim 100$ GeV and $T_{\text{RH}} = 5$ GeV one requires $g_\phi = \mathcal{O}(10^{-1})$ in order to satisfy

the observed relic density while fixing $m_\eta = 60$ GeV and $\sin \beta = 0.1$. We also discuss the relevant theoretical and experimental constraints that restrict the scalar masses and the mixing angle. Finally, we perform exhaustive numerical scans to obtain the contours that satisfy the observed relic density in the m_{DM} vs. g_ϕ plane for different values of T_{RH} and benchmark values of other model parameters. We also discuss the direct detection constraints on the same coupling from experiments like LZ and PandaX-4T. We find that the DM masses with the ratio $M_{\text{DM}}/T_{\text{RH}} \sim 15 - 20$ are excluded from existing direct searches. For completeness, we also discuss the indirect detection constraints, and we find that the most stringent bounds apply on the DM annihilation channel to W^+W^- . However, indirect detection constraints are found to be significantly weaker compared to the direct search limits. Despite the stringent constraints, there still exists a viable parameter space that can accommodate a stable DM with the correct relic density. Moreover, any new signal in future experiments can offer new insights in such a scenario, as the DM mass and the reheating temperature pose a strong correlation. Thus, the freeze in VDM at low reheating temperatures in such $SU(2)_{\text{HS}}$ setup may lead to significant insights into the experimental and phenomenological possibilities of DM model building. In the future, extending VDM frameworks to larger hidden-sector gauge groups, such as $SU(N)_{\text{HS}}$ with $N \geq 3$ [38], could significantly broaden the paradigm and open up a rich landscape of novel dark matter phenomenology and model-building possibilities.

Acknowledgement

SG acknowledges the support of a postdoctoral fellowship from IIT Kharagpur (Offer no. - IIT/PDF/2025/PH/23). X.-G.H was supported by the Fundamental Research Funds for the Central Universities, by the National Natural Science Foundation of the People's Republic of China (Nos. 12090064, 12375088, and W2441004). SJ acknowledges the financial support from the National Natural Science Foundation of China (12425506 and 12375101) and the State Key Laboratory of Dark Matter Physics.

A Parametrization

Here we present the parametrization of the quartic couplings in terms of the masses of the physical scalars. If $m_\eta > m_h$, then :

$$m_{h,\eta}^2 = \lambda_H v^2 + \lambda_\phi v_\phi^2 \mp (\lambda_\phi v_\phi^2 - \lambda_H v^2) / \cos 2\beta, \quad (\text{A.1})$$

and the quartic couplings can be expressed as

$$\lambda_H = \frac{m_h^2}{2v^2} \cos^2 \beta + \frac{m_\eta^2}{2v^2} \sin^2 \beta, \quad \lambda_\phi = \frac{m_h^2}{2v_\phi^2} \sin^2 \beta + \frac{m_\eta^2}{2v_\phi^2} \cos^2 \beta, \quad \lambda_{\phi H} = \frac{\sin 2\beta}{2vv_\phi} (m_\eta^2 - m_h^2). \quad (\text{A.2})$$

If $m_\eta < m_h$, then :

$$m_{h,\eta}^2 = \lambda_H v^2 + \lambda_\phi v_\phi^2 \pm (\lambda_\phi v_\phi^2 - \lambda_H v^2) / \cos 2\beta, \quad (\text{A.3})$$

and the quartic couplings

$$\lambda_H = \frac{m_h^2}{2v^2} \sin^2 \beta + \frac{m_\eta^2}{2v^2} \cos^2 \beta, \quad \lambda_\phi = \frac{m_h^2}{2v_\phi^2} \cos^2 \beta + \frac{m_\eta^2}{2v_\phi^2} \sin^2 \beta, \quad \lambda_{\phi H} = \frac{\sin 2\beta}{2vv_\phi} (m_h^2 - m_\eta^2). \quad (\text{A.4})$$

B Cross-sections for $h_i h_j \rightarrow XX$

The amplitude for the process $h_i h_j \rightarrow XX$ receives contributions from contact interaction, s -channel scalar exchange and, when allowed by the cubic $h_i XX$ vertices, t - and u -channel vector exchange:

$$\mathcal{M}_{ij} = \mathcal{M}_{ij}^{\text{cont}} + \mathcal{M}_{ij}^s + \mathcal{M}_{ij}^t + \mathcal{M}_{ij}^u. \quad (\text{B.1})$$

The required vector X -scalar couplings are

$$g_{hXX} = -\frac{g_\phi^2 v_\phi}{4} \sin \beta, \quad g_{\eta XX} = \frac{g_\phi^2 v_\phi}{4} \cos \beta, \quad (\text{B.2})$$

The total cross section can be written as,

$$\begin{aligned} \sigma_{h_i h_j \rightarrow XX} = \frac{1}{64\pi s} \sqrt{\frac{s(s-4m_X^2)}{(s-m_{h_i}^2-m_{h_j}^2)^2-4m_{h_i}^2 m_{h_j}^2}} & \left[C_0 + C_1 \frac{1}{\mathcal{A}^2 - \mathcal{B}^2} + C_2 \frac{1}{\mathcal{B}} \ln \left(\frac{|\mathcal{A} + \mathcal{B}|}{|\mathcal{A} - \mathcal{B}|} \right) \right. \\ & \left. + C_3(3\mathcal{A}^2 + \mathcal{B}^2) + C_4 \mathcal{A} + C_5 \mathcal{A}(\mathcal{A}^2 + \mathcal{B}^2) \right] \end{aligned} \quad (\text{B.3})$$

For $h(k_1)h(k_2) \rightarrow X(p_1)X(p_2)$ the aforementioned terms will be,

$$\begin{aligned} \mathcal{A} &= \frac{2m_h^2 - s}{2m_X^2}, \quad \mathcal{B} = \frac{1}{2m_X^2} \sqrt{(s-4m_h^2)(s-4m_X^2)}, \\ C_s &= \frac{\cos \beta \rho_2 v_\phi}{s - m_\eta^2 + im_\eta \Gamma_\eta} - \frac{\sin \beta \rho_h v_\phi}{s - m_h^2 + im_h \Gamma_h} + \sin^2 \beta \end{aligned} \quad (\text{B.4})$$

$$\begin{aligned} C_0 &= 2 \left[\frac{|C_s|^2}{v_\phi^4} (12m_X^4 - 4sm_X^2 + s^2) + \frac{4\sin^4 \beta}{v_\phi^4} (-4m_X^4 + 4m_X^2 m_h^2 - 6m_X^2 s + m_h^4 + 2m_h^2 s) \right. \\ & \left. + \frac{8\sin^2 \beta \Re(C_s)}{v_\phi^4} (-2m_X^2 m_h^2 + 2m_X^2 s - m_h^2 s) \right] \end{aligned} \quad (\text{B.5})$$

$$C_1 = \frac{4\sin^4 \beta}{v_\phi^4 m_X^4} (48m_X^8 - 32m_X^6 m_h^2 + 24m_X^4 m_h^4 - 16m_X^4 m_h^2 s + 4m_X^4 s^2 - 8m_X^2 m_h^6 + 4m_X^2 m_h^4 s + m_h^8)$$

$$\begin{aligned} C_2 &= 4 \left[\frac{\sin^4 \beta}{m_X^2 v_\phi^4 (s-2m_h^2)} (-48m_X^8 + 32m_X^6 m_h^2 - 8m_X^4 m_h^4 + 4m_X^4 s^2 - 8m_X^2 m_h^6 + 4m_X^2 m_h^2 s^2 \right. \\ & \left. - 2m_X^2 s^3 + 3m_h^8 - m_h^4 s^2) + \frac{\sin^2 \beta \Re(C_s)}{m_X^2 v_\phi^4} (24m_X^6 + 2m_X^2 (m_h^2 - s)^2 + m_h^4 s - 4m_X^4 (2m_h^2 + s)) \right] \end{aligned} \quad (\text{B.6})$$

$$C_3 = -\frac{1}{4} g_\phi^4 \sin^4 \beta$$

$$\begin{aligned} C_4 &= \frac{8m_X^2 \sin^2 \beta}{v_\phi^4 (2m_h^2 - s)} \left[\sin^2 \beta (8m_X^4 - 8m_X^2 m_h^2 + 8m_X^2 s + 2m_h^4 - 4m_h^2 s + s^2) \right. \\ & \left. + \Re(C_s) (4m_X^2 m_h^2 - 2m_X^2 s + 2m_h^2 s - s^2) \right] \end{aligned} \quad (\text{B.7})$$

$$C_5 = \frac{8\sin^4 \beta m_X^6}{v_\phi^4 (2m_h^2 - s)}$$

For $\eta(k_1)\eta(k_2) \rightarrow X(p_1)X(p_2)$ the terms in eq.(B.3) will be

$$\begin{aligned} \mathcal{A} &= \frac{2m_\eta^2 - s}{2m_X^2}, \quad \mathcal{B} = \frac{1}{2m_X^2} \sqrt{(s - 4m_\eta^2)(s - 4m_X^2)}, \\ \mathcal{C}_s &= \cos^2 \beta + \frac{\rho_\eta v_\phi \sin \beta}{s - m_\eta^2 + im_\eta \Gamma_\eta} - \frac{\rho_1 v_\phi \cos \beta}{s - m_h^2 + im_h \Gamma_h} \end{aligned} \quad (\text{B.8})$$

$$\begin{aligned} \mathcal{C}_0 &= 2 \left[\frac{|C_s|^2}{v_\phi^4} (12m_X^4 - 4sm_X^2 + s^2) + \frac{4 \cos^4 \beta}{v_\phi^4} (-4m_X^4 + 4m_X^2 m_\eta^2 - 6m_X^2 s + m_\eta^4 + 2m_\eta^2 s) \right. \\ &\quad \left. + \frac{8 \cos^2 \beta \Re(C_s)}{v_\phi^4} (-2m_X^2 m_\eta^2 + 2m_X^2 s - m_\eta^2 s) \right] \\ \mathcal{C}_1 &= \frac{4 \cos^4 \beta}{v_\phi^4 m_X^4} (48m_X^8 - 32m_X^6 m_\eta^2 + 24m_X^4 m_\eta^4 - 16m_X^4 m_\eta^2 s + 4m_X^4 s^2 - 8m_X^2 m_\eta^6 + 4m_X^2 m_\eta^4 s + m_\eta^8) \end{aligned} \quad (\text{B.9})$$

$$\begin{aligned} \mathcal{C}_2 &= 4 \left[\frac{\cos^4 \beta}{m_X^2 v_\phi^4 (s - 2m_\eta^2)} (-48m_X^8 + 32m_X^6 m_\eta^2 - 8m_X^4 m_\eta^4 + 4m_X^4 s^2 - 8m_X^2 m_\eta^6 + 4m_X^2 m_\eta^2 s^2 \right. \\ &\quad \left. - 2m_X^2 s^3 + 3m_\eta^8 - m_\eta^4 s^2) + \frac{\cos^2 \beta \Re(C_s)}{m_X^2 v_\phi^4} (24m_X^6 + 2m_X^2 (m_\eta^2 - s)^2 + m_\eta^4 s - 4m_X^4 (2m_\eta^2 + s)) \right] \end{aligned}$$

$$\begin{aligned} \mathcal{C}_3 &= -\frac{1}{4} g_\phi^4 \cos^4 \beta \\ \mathcal{C}_4 &= \frac{8m_X^2 \cos^2 \beta}{v_\phi^4 (2m_\eta^2 - s)} [\cos^2 \beta (8m_X^4 - 8m_X^2 m_\eta^2 + 8m_X^2 s + 2m_\eta^4 - 4m_\eta^2 s + s^2) \\ &\quad + \Re(C_s) (4m_X^2 m_\eta^2 - 2m_X^2 s + 2m_\eta^2 s - s^2)] \\ \mathcal{C}_5 &= \frac{8 \cos^4 \beta m_X^6}{v_\phi^4 (2m_\eta^2 - s)} \end{aligned} \quad (\text{B.10})$$

On the other hand, for the process $h(k_1)\eta(k_2) \rightarrow X(p_1)X(p_2)$ the terms in eq.(B.3) will be,

$$\mathcal{A} = \frac{m_h^2 + m_\eta^2 - s}{2m_X^2}, \quad \mathcal{B} = \frac{1}{2m_X^2} \sqrt{1 - \frac{4m_X^2}{s}} \sqrt{(s - m_h^2 - m_\eta^2)^2 - 4m_h^2 m_\eta^2}, \quad (\text{B.11})$$

$$\begin{aligned} \mathcal{C}_s &= (-\sin \beta \cos \beta + \frac{\rho_1 \cos \beta v_\phi}{s - m_\eta^2 + im_\eta \Gamma_\eta} - \frac{\rho_2 \sin \beta v_\phi}{s - m_h^2 + im_h \Gamma_h}) \\ \mathcal{C}_0 &= 2 \frac{|C_s|^2}{v_\phi^4} (s^2 - 4m_X^2 s + 12m_X^4) \\ &\quad + \frac{\sin^2 2\beta}{v_\phi^4} (-8m_X^4 + 4m_X^2 m_\eta^2 + m_\eta^4 + 4m_X^2 m_h^2 + m_h^4 - 12m_X^2 s + 2m_\eta^2 s + 2m_h^2 s) \\ &\quad + 4\Re(C_s) \frac{\sin 2\beta}{v_\phi^4} (2m_X^2 m_\eta^2 + 2m_X^2 m_h^2 - 4m_X^2 s + m_\eta^2 s + m_h^2 s) \\ \mathcal{C}_1 &= \frac{\sin^2 2\beta}{m_X^4 v_\phi^4} (48m_X^8 - 16m_X^6 m_\eta^2 - 16m_X^6 m_h^2 + 8m_X^4 m_\eta^4 + 8m_X^4 m_\eta^2 m_h^2 - 8m_X^4 m_\eta^2 s + 8m_X^4 m_h^4 \\ &\quad - 8m_X^4 m_h^2 s + 4m_X^4 s^2 - 4m_X^2 m_\eta^4 m_h^2 - 4m_X^2 m_\eta^2 m_h^4 + 4m_X^2 m_\eta^2 m_h^2 s + m_\eta^4 m_h^4), \end{aligned} \quad (\text{B.12})$$

$$\begin{aligned}
\mathcal{C}_2 &= \frac{2\Re(C_s) \sin 2\beta}{m_X^2 v_\phi^4} (-24m_X^6 + 4m_X^4 m_\eta^2 + 4m_X^4 m_h^2 + 4m_X^4 s - 2m_X^2 m_\eta^4 + 2m_X^2 m_\eta^2 m_h^2 + 2m_X^2 m_\eta^2 s - 2m_X^2 m_h^4 \\
&\quad + 2m_X^2 m_h^2 s - 2m_X^2 s^2 - m_\eta^2 m_h^2 s), \\
&\quad + \frac{\sin^2 2\beta}{m_X^2 v_\phi^4 (m_h^2 + m_\eta^2 - s)} (48m_X^8 - 16m_X^6 m_\eta^2 + 8m_X^4 m_\eta^4 - 2m_X^2 m_\eta^6 \\
&\quad - 16m_X^6 m_h^2 - 8m_X^4 m_\eta^2 m_h^2 + 6m_X^2 m_\eta^4 m_h^2 - m_\eta^6 m_h^2 + 8m_X^4 m_h^4 + 6m_X^2 m_\eta^2 m_h^4 \\
&\quad - m_\eta^4 m_h^4 - 2m_X^2 m_h^6 - m_\eta^2 m_h^6 + 2m_X^2 m_\eta^4 s - 4m_X^2 m_\eta^2 m_h^2 s + 2m_X^2 m_h^4 s \\
&\quad - 4m_X^4 s^2 - 2m_X^2 m_\eta^2 s^2 - 2m_X^2 m_h^2 s^2 + m_\eta^2 m_h^2 s^2 + 2m_X^2 s^3) \\
\mathcal{C}_3 &= -\frac{1}{4} g_\phi^4 \cos^2 \beta \sin^2 \beta \\
\mathcal{C}_4 &= -\frac{4 \sin 2\beta \Re(C_s) m_X^2}{v_\phi^4} (2m_X^2 + s) - \frac{2 \sin^2 2\beta m_X^2}{v_\phi^4} (m_\eta^2 + m_h^2) + \frac{2 \sin^2 2\beta m_X^2}{v_\phi^4 (m_h^2 + m_\eta^2 - s)} \\
&\quad (8m_X^4 - 4m_X^2 m_h^2 + m_h^4 - 4m_X^2 m_\eta^2 + 4m_h^2 m_\eta^2 + m_\eta^4 + 8m_X^2 s - 3m_h^2 s - 3m_\eta^2 s + s^2) \quad (\text{B.13}) \\
\mathcal{C}_5 &= \frac{2m_X^6 \sin^2 2\beta}{(m_h^2 + m_\eta^2 - s) v_\phi^4}
\end{aligned}$$

C Interaction Lagrangian of scalar sector

In the mass eigenstate basis, the interaction terms in the Lagrangian is :

$$\mathcal{L} \supset -\frac{1}{6} \rho_h h^3 - \frac{1}{6} \rho_\eta \eta^3 - \frac{1}{2} \rho_1 \eta^2 h - \frac{1}{2} \rho_2 h^2 \eta \quad (\text{C.1})$$

where the scalar trilinear couplings are given by

$$\begin{aligned}
\rho_1 &= -6\lambda_\phi v_\phi \cos^2 \beta \sin \beta + 6\lambda_H v \sin^2 \beta \cos \beta \\
&\quad + \lambda_{\phi H} (v \cos^3 \beta - v_\phi \sin^3 \beta - 2v \cos \beta \sin^2 \beta + 2v_\phi \cos^2 \beta \sin \beta), \quad (\text{C.2})
\end{aligned}$$

$$\begin{aligned}
\rho_2 &= 6\lambda_\phi v_\phi \sin^2 \beta \cos \beta + 6\lambda_H v \cos^2 \beta \sin \beta \\
&\quad + \lambda_{\phi H} (v \sin^3 \beta + v_\phi \cos^3 \beta - 2v \cos^2 \beta \sin \beta - 2v_\phi \sin^2 \beta \cos \beta), \quad (\text{C.3})
\end{aligned}$$

$$\rho_\eta = 6\lambda_\phi v_\phi \cos^3 \beta + 6\lambda_H v \sin^3 \beta + 3\lambda_{\phi H} \cos \beta \sin \beta (v \cos \beta + v_\phi \sin \beta), \quad (\text{C.4})$$

$$\rho_h = -6\lambda_\phi v_\phi \sin^3 \beta + 6\lambda_H v \cos^3 \beta + 3\lambda_{\phi H} \cos \beta \sin \beta (v \sin \beta - v_\phi \cos \beta). \quad (\text{C.5})$$

References

- [1] F. Zwicky, *Die Rotverschiebung von extragalaktischen Nebeln*, *Helv. Phys. Acta* **6** (1933) 110–127.
- [2] V. C. Rubin and W. K. Ford, Jr., *Rotation of the Andromeda Nebula from a Spectroscopic Survey of Emission Regions*, *Astrophys. J.* **159** (1970) 379–403.
- [3] D. Clowe, M. Bradac, A. H. Gonzalez, M. Markevitch, S. W. Randall, C. Jones et al., *A direct empirical proof of the existence of dark matter*, *Astrophys. J. Lett.* **648** (2006) L109–L113, [[astro-ph/0608407](#)].
- [4] PLANCK collaboration, N. Aghanim et al., *Planck 2018 results. VI. Cosmological parameters*, *Astron. Astrophys.* **641** (2020) A6, [[1807.06209](#)].

- [5] G. Jungman, M. Kamionkowski and K. Griest, *Supersymmetric dark matter*, *Phys. Rept.* **267** (1996) 195–373, [[hep-ph/9506380](#)].
- [6] G. Bertone, D. Hooper and J. Silk, *Particle dark matter: Evidence, candidates and constraints*, *Phys. Rept.* **405** (2005) 279–390, [[hep-ph/0404175](#)].
- [7] J. L. Feng, *Dark Matter Candidates from Particle Physics and Methods of Detection*, *Ann. Rev. Astron. Astrophys.* **48** (2010) 495–545, [[1003.0904](#)].
- [8] G. Arcadi, M. Dutra, P. Ghosh, M. Lindner, Y. Mambrini, M. Pierre et al., *The waning of the WIMP? A review of models, searches, and constraints*, *Eur. Phys. J. C* **78** (2018) 203, [[1703.07364](#)].
- [9] L. Roszkowski, E. M. Sessolo and S. Trojanowski, *WIMP dark matter candidates and searches—current status and future prospects*, *Rept. Prog. Phys.* **81** (2018) 066201, [[1707.06277](#)].
- [10] PANDAX-II collaboration, X. Cui et al., *Dark Matter Results From 54-Ton-Day Exposure of PandaX-II Experiment*, *Phys. Rev. Lett.* **119** (2017) 181302, [[1708.06917](#)].
- [11] PANDAX collaboration, H. Zhang et al., *Dark matter direct search sensitivity of the PandaX-4T experiment*, *Sci. China Phys. Mech. Astron.* **62** (2019) 31011, [[1806.02229](#)].
- [12] XENON collaboration, E. Aprile et al., *Projected WIMP sensitivity of the XENONnT dark matter experiment*, *JCAP* **11** (2020) 031, [[2007.08796](#)].
- [13] H.E.S.S. collaboration, H. Abdallah et al., *Search for dark matter annihilations towards the inner Galactic halo from 10 years of observations with H.E.S.S.*, *Phys. Rev. Lett.* **117** (2016) 111301, [[1607.08142](#)].
- [14] ATLAS collaboration, M. Aaboud et al., *Search for dark matter and other new phenomena in events with an energetic jet and large missing transverse momentum using the ATLAS detector*, *JHEP* **01** (2018) 126, [[1711.03301](#)].
- [15] L. J. Hall, K. Jedamzik, J. March-Russell and S. M. West, *Freeze-In Production of FIMP Dark Matter*, *JHEP* **03** (2010) 080, [[0911.1120](#)].
- [16] N. Bernal, M. Heikinheimo, T. Tenkanen, K. Tuominen and V. Vaskonen, *The Dawn of FIMP Dark Matter: A Review of Models and Constraints*, *Int. J. Mod. Phys. A* **32** (2017) 1730023, [[1706.07442](#)].
- [17] C. Cosme, F. Costa and O. Lebedev, *Freeze-in at stronger coupling*, *Phys. Rev. D* **109** (2024) 075038, [[2306.13061](#)].
- [18] M. Kawasaki, K. Kohri and N. Sugiyama, *MeV scale reheating temperature and thermalization of neutrino background*, *Phys. Rev. D* **62** (2000) 023506, [[astro-ph/0002127](#)].
- [19] K. Ichikawa, M. Kawasaki and F. Takahashi, *The Oscillation effects on thermalization of the neutrinos in the Universe with low reheating temperature*, *Phys. Rev. D* **72** (2005) 043522, [[astro-ph/0505395](#)].
- [20] J. Silva-Malpartida, N. Bernal, J. Jones-Pérez and R. A. Lineros, *From WIMPs to FIMPs with low reheating temperatures*, *JCAP* **09** (2023) 015, [[2306.14943](#)].
- [21] F. Koutroulis, O. Lebedev and S. Pokorski, *Gravitational production of sterile neutrinos*, *JHEP* **04** (2024) 027, [[2310.15906](#)].
- [22] S. Khan, J. Kim and H. M. Lee, *Higgs portal vector dark matter at a low reheating temperature*, *JCAP* **06** (2025) 040, [[2503.17621](#)].
- [23] G. Arcadi, F. Costa, A. Goudelis and O. Lebedev, *Higgs portal dark matter freeze-in at stronger coupling: observational benchmarks*, *JHEP* **07** (2024) 044, [[2405.03760](#)].

- [24] K. K. Boddy, K. Freese, G. Montefalcone and B. Shams Es Haghi, *Minimal dark matter freeze-in with low reheating temperatures and implications for direct detection*, *Phys. Rev. D* **111** (2025) 063537, [[2405.06226](#)].
- [25] G. Arcadi, D. Cabo-Almeida and O. Lebedev, *Z'-mediated dark matter freeze-in at stronger coupling*, *Phys. Lett. B* **861** (2025) 139268, [[2409.02191](#)].
- [26] G. Bélanger, N. Bernal and A. Pukhov, *Z'-mediated dark matter with low-temperature reheating*, *JHEP* **03** (2025) 079, [[2412.12303](#)].
- [27] P. Arias, B. Díaz Sáez, L. Duarte, J. Jones-Pérez, W. Rodriguez and D. Z. Herrera, *Probing displaced (dark)photons from low reheating freeze-in at the LHC*, *JHEP* **01** (2026) 135, [[2507.15930](#)].
- [28] N. Bernal, S. Mukherjee and J. Unwin, *Minimal Freeze-in Dark Matter: Reviving electroweak doublet dark matter with Boltzmann suppressed freeze-in*, [2602.10112](#).
- [29] T. Hambye, *Hidden vector dark matter*, *JHEP* **01** (2009) 028, [[0811.0172](#)].
- [30] N. Baouche, A. Ahriche, G. Faisel and S. Nasri, *Phenomenology of the hidden SU(2) vector dark matter model*, *Phys. Rev. D* **104** (2021) 075022, [[2105.14387](#)].
- [31] PARTICLE DATA GROUP collaboration, S. Navas et al., *Review of particle physics*, *Phys. Rev. D* **110** (2024) 030001.
- [32] ATLAS, CMS collaboration, G. Aad et al., *Measurements of the Higgs boson production and decay rates and constraints on its couplings from a combined ATLAS and CMS analysis of the LHC pp collision data at $\sqrt{s} = 7$ and 8 TeV*, *JHEP* **08** (2016) 045, [[1606.02266](#)].
- [33] LZ collaboration, J. Aalbers et al., *Dark Matter Search Results from 4.2 Tonne-Years of Exposure of the LUX-ZEPLIN (LZ) Experiment*, *Phys. Rev. Lett.* **135** (2025) 011802, [[2410.17036](#)].
- [34] PANDAX-4T collaboration, Y. Meng et al., *Dark Matter Search Results from the PandaX-4T Commissioning Run*, *Phys. Rev. Lett.* **127** (2021) 261802, [[2107.13438](#)].
- [35] A. et. al., *Measurement of separate cosmic-ray electron and positron spectra with the fermi large area telescope*, *Physical Review Letters* **108** (Jan., 2012) .
- [36] F. Calore, M. Cirelli, L. Derome, Y. Genolini, D. Maurin, P. Salati et al., *AMS-02 antiprotons and dark matter: Trimmed hints and robust bounds*, *SciPost Phys.* **12** (2022) 163, [[2202.03076](#)].
- [37] DARWIN collaboration, J. Aalbers et al., *DARWIN: towards the ultimate dark matter detector*, *JCAP* **11** (2016) 017, [[1606.07001](#)].
- [38] M. Frigerio, N. Grimbaum-Yamamoto and T. Hambye, *Dark matter from the centre of SU(N)*, *SciPost Phys.* **15** (2023) 177, [[2212.11918](#)].